Sensors and Materials, Vol. 38, No. 6 (2026) 2953–2976
MYU Tokyo

S & M 4480

Dual-band Noncontact Doppler Radar System for Pulse Measurement with K- and X-Band Frequencies

Wei-Lung Wu*

Department of Aviation Communication and Electronics, Air Force Institute of Technology,
Kaohsiung 820, Taiwan

(Received February 9, 2026; accepted March 16, 2026)

Keywords: dual-band radar, Doppler/microdisplacement, pulse measurement, 24 GHz phase antenna, 12 GHz horn antenna, I/Q quadrature receiver, PLL frequency synthesizer

In this study, we developed a dual-frequency radar measurement system that exploits the Doppler effect and microdisplacement-induced echo phase variations. The system detects targets by using two frequency bands simultaneously: the 24 GHz (phased antenna array) and 12 GHz (conical antenna array) bands. This dual-frequency radar system enables the precise, noncontact measurement of physiological signals, including heartbeat and respiration, as well as minor variations in pulse and vascular contraction. Compared with single-frequency, unidirectional radar measurements, the proposed system's measurements showed inter-band agreement during repeated validation. Dual-frequency measurement enables the cross-comparison and verification of data, exhibiting high consistency while optimizing the trade-off among sensitivity, penetration, measurement range, and robustness to body motion. The proposed system demonstrates the feasibility of noncontact, dual-frequency radar-based physiological monitoring under minimal pulse variation. Pearson correlation coefficient (r) analysis was used to quantify the linear consistency between the 12 and 24 GHz measurements, yielding an r value of 0.82096, a 95% confidence interval of 0.80756–0.83351 (estimated using Fisher's z-transform), and a two-tailed p value considerably below 0.001. These results indicate that the dual-frequency radar sequences are highly synchronized in amplitude trends and exhibit strong linear consistency, providing a reliable basis for cross-validation and data fusion.

1. Introduction

The application of noncontact physiological measurement technologies has grown rapidly in various areas, such as smart health care, telecare, home-based health monitoring, and disaster response.(1) Physiologically, a pulse refers to the arterial pulsation induced by cardiac contraction. In signal processing, this phenomenon is commonly described as a pulse, an impulse, or a pulse wave, representing a signal characterized by rapid, transient changes associated with cardiac activity.(2) The waveform recorded during pulse measurement reflects these instantaneous

---

*Corresponding author: e-mail: u0415905@first.nkust.edu.tw
https://doi.org/10.18494/SAM6278

ISSN 0914-4935
https://myukk.org/

pulsations and corresponds closely to cardiac rhythms. Cardiac activity is divided into distinct electrocardiogram components, including the P wave, QRS complex, and T wave, which represent different phases of cardiac electrical activity. Given the close correspondence between cardiac rhythms and pulsations, pulse measurement supports not only heart rate (HR) and pulse rate (PR) monitoring but also the estimation of vascular elasticity, circulatory status, and autonomic nervous system modulation. Such physiological information has practical value for early disease prevention and health risk assessment. Traditional pulse measurement approaches, such as photoplethysmography and electrocardiography (ECG), primarily rely on contact-based sensors.(3) However, contact-based approaches frequently encounter limitations during prolonged wear, under compromised skin conditions (e.g., perspiration, dryness, or eczema), during physical activity or nocturnal movement, and when use is constrained by protective equipment or heavy clothing.(4) Sustained skin–sensor contact and friction often result in user discomfort and reduce signal stability. Moreover, contact-based measurement may impose psychological pressure or discomfort, a concern that is particularly pronounced in the clinical physiological monitoring of older populations, including community-dwelling elderly individuals and long-term care recipients, as well as in monitoring conducted in public environments.(5) These factors have limited the feasibility of conducting accurate PR measurements simultaneously for large numbers of people. Consequently, techniques capable of acquiring physiological signals and pulse-related microdisplacement signals without direct skin contact have begun to be developed. In this context, the use of millimeter-wave frequencies (which are widely adopted because of their broad usable bandwidth and high measurement accuracy) and their implementation in millimeter-wave radar systems have gradually attracted increasing attention. Radar-based physiological measurement systems offer advantages such as noncontact operation, clothing penetration, and remote sensing capability. However, the practical deployment of these systems is restricted by several critical challenges. First, the magnitudes of human microdisplacements are extremely small; pulse-related signals are often associated with millimeter- or submillimeter-scale microdisplacements and exhibit high sensitivity to front-end phase noise, in-phase and quadrature (I/Q) imbalance, DC offset, and noise floor limitations. Second, unavoidable motion-related interference arises during measurement, including wrist posture changes, respiration-induced hand movements, and substantial angular deviations between the target and the radar. These factors tend to obscure weak pulse components and may introduce spectral aliasing or waveform distortion. Third, radar systems operating in different frequency bands differ in terms of their penetration capability, scattering characteristics, antenna beamwidth, and phase sensitivity to microdisplacements. In particular, the operating frequency of 24 GHz (adopted in the proposed system) generally offers high sensitivity to phase variations and high near-range microdisplacement resolution but also exhibits relatively high susceptibility to occlusion and posture variation.(6) By contrast, lower frequencies, such as 12 GHz, typically provide deeper penetration and are often more stable under mild motion; however, they generally exhibit lower microdisplacement sensitivity (smaller phase change per unit microdisplacement) and reduced spatial selectivity, which may increase susceptibility to clutter and multipath interference. Collectively, these differences indicate that integrating dual-frequency measurements may enable a more effective trade-off between sensitivity and stability in signal analysis.(7)

On the basis of the aforementioned discussion, we developed an integrated dual-band system for pulse measurement. The 24 GHz band (K-band) serves as the primary phase-sensing channel of this system, which exploits the high phase sensitivity of this band to accurately capture pulse-induced microdisplacement phase variations. The 12 GHz band (X-band) functions as an auxiliary channel for validation and deeper sensing. The proposed system leverages the strong penetration capability of this band to measure pulse-related signals accurately over a relatively large depth. Through simultaneous dual-band operation, the proposed system can realize highly accurate noncontact radar-based pulse measurement. The core principle of the proposed system is related to signal acquisition and analysis across the K- and X-bands. Signals measured at 24 GHz serve as the primary analytical input, whereas signals obtained at 12 GHz provide supplementary measurements for cross-comparison and verification. This dual-band strategy improves measurement coverage, penetration performance, and echo energy stability while enabling cross-validation and signal analysis under specific postural or environmental conditions, thereby enhancing overall measurement robustness and usability. The proposed system consists of two main components: a K-band (24 GHz) phased antenna array and an X-band (12 GHz) conical antenna array. The K-band antenna array uses separate transmitter (Tx) and receiver (Rx) paths to acquire and mix phase information. The X-band antenna array also uses independent Tx and Rx paths to enhance directivity and gain, thereby improving echo signal quality prior to mixing. Although the measurement approaches of both arrays are based on Doppler and microdisplacement principles, differences in their antenna structures and frequency-dependent characteristics allow the two bands to complement one another within the proposed system. The primary objective of the proposed system is to measure phase differences to enable the rapid interpretation of the Doppler shifts induced by microdisplacement changes.(8) Sufficient measurement sensitivity is essential for detecting weak pulsations at the skin surface, such as minor undulations of the vascular wall caused by radial artery pulsation at the wrist. These pulsations manifest as time-varying changes in echo phase signals and frequency when microdisplacements occur within the radar-illuminated region. Doppler radar characteristics permit the use of higher peak power (PR/HR is estimated within 0.8–2.0 Hz 48–120 bpm and RR, when applicable, within 0.1–0.5 Hz 6–30 bpm) to enhance long-range sensing capability. However, a continuous-wave (CW) architecture must be adopted for each antenna array in near-range physiological measurement, in which the target distance remains relatively fixed and the focus lies on frequency modulation, microdisplacement, and phase variation. To support this near-range application, the proposed system has a high-stability configuration that integrates millimeter-wave voltage-controlled oscillators (VCOs), high-sensitivity low-pass filters (LPFs), and feedback signal paths, with subsequent I/Q demodulation processing. Although this hardware configuration increases system complexity and requires the resolution of multiple technical challenges, iterative testing confirmed the stability of the proposed system. Consequently, the system provides comprehensive measurement information and achieves high sensitivity. Under relatively stable operating conditions, the physiological signals acquired by the system correspond well to measurement metrics commonly adopted in contemporary physiological monitoring.

2. System Overview and Measurement Principles

In this study, we developed a dual-band, noncontact radar-based pulse measurement system, integrating complementary measurement strategies across the hardware and software components to implement Doppler- and microdisplacement-based phase demodulation. The overall system is organized into four functional regions: a radar front-end architecture (RADAR in Fig. 1), a hardware control and data acquisition (DAQ) module (Hardware), a circuit integration module (Circuit Integration), and a signal processing software module (Software). The hardware module manages dual-band radar transmission and reception through two antenna arrays (i.e., the 24 and 12 GHz arrays) and captures I/Q signals. The software module performs real-time control and data streaming by using LabVIEW and conducts signal denoising and HR or PR estimation by employing MATLAB. The backend signal processing workflow involves the following steps in sequence: I/Q demodulation, denoising and motion artifact removal, frequency and waveform estimation, and final output of physiological parameters such as PR. The modular architecture of the proposed system is illustrated in Fig. 1.

The hardware, circuit integration, and software modules are described as follows:

a) Hardware module: The hardware module contains three components, namely, antenna arrays, a DAQ device, and circuit integration. The ERAVANT-SAM-2432432212-KF-L1 phased antenna array (Eravant, Torrance, CA, USA) is used to conduct measurements in the K-band (24 GHz), whereas the ERAVANT-SWC-90SF-R5 conical antenna array is used to perform measurements in the X-band (12 GHz).

b) Circuit-integration submodule: The circuit integration module transmits the signals acquired by the antenna arrays to the hardware module (within the hardware module). The hardware module manages overall system control, including frequency synthesizer operation, radar output frequency control, measurement initiation and termination, parameter configuration (sampling rate, measurement duration, and synchronized signal acquisition), and data management and storage.

c) Software module: The software workflow consists of two main stages. First, signal acquisition, measurement control, and I/Q/phase demodulation were implemented in LabVIEW to acquire signals and perform measurement control, synchronized sampling, data

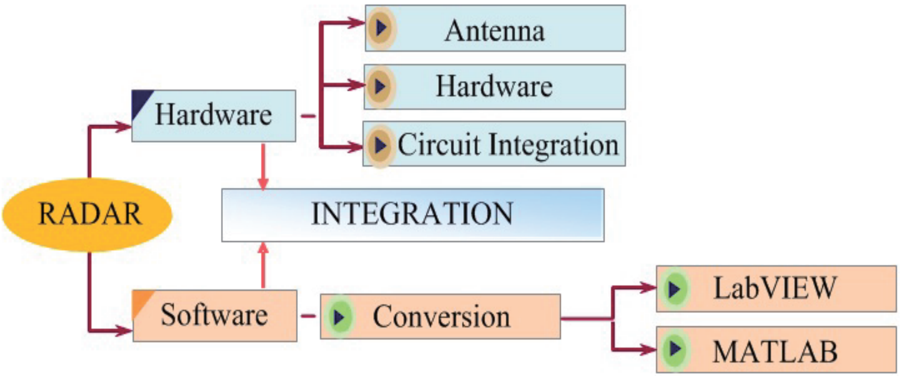

Fig. 1. (Color online) Measurement system architecture diagram.

packaging, and storage. Subsequently, MATLAB is employed for system conversion and computation, signal processing, feature extraction, and parameter estimation, enabling offline or near-real-time signal processing and the output of physiological indicators.

After signal acquisition by the antennas in the hardware module, the circuit-integration submodule processes the received signals to achieve isolation between Tx and Rx paths. Separate Tx and Rx antennas are employed with circuit-level isolation, attenuation, and filtering designs to mitigate DC drift and I/Q distortion at the receiver. Through an I/Q demodulation interface, the received echoes are converted into I- and Q-phase baseband signals with a phase difference of 90° and then output to the DAQ device (PXIe-6124). Subsequently, calibration and verification procedures are conducted to correct I/Q offset (DC offset), gain imbalance, and quadrature errors, thereby reducing phase estimation inaccuracies (Fig. 2).

In the conversion stage, overall system control and status monitoring are performed using a PC or a PXIe-based host controller. The proposed system leverages its DAQ functionality to capture baseband I/Q signals by using a PXIe platform that comprises the following components: a PXIe-1073 chassis or platform (providing the system backplane and module power), a PXIe-6124 multichannel analog input module (for acquiring I- and Q-phase signals), a PXIe-8361 host interface and data transfer module (for system-level data exchange), and a BNC-2110 signal terminal block (facilitating the convenient connection of I/Q signals to DAQ channels). The primary function of the DAQ device is to acquire demodulated dual-band I/Q signals with high stability, synchronicity, and resolution, thereby providing reliable input data for backend software-based phase demodulation and spectral analysis.

The circuit integration module connects a frequency synthesizer, frequency division and distribution circuits, mixers, and transmit–receive signal chains, enabling simultaneous dual-band operation and the generation of I/Q baseband signals suitable for acquisition. Within the DAQ sampling framework, the I/Q receiver downconverts the received echoes to baseband or intermediate frequency, producing I- and Q-phase outputs. The data acquisition platform is

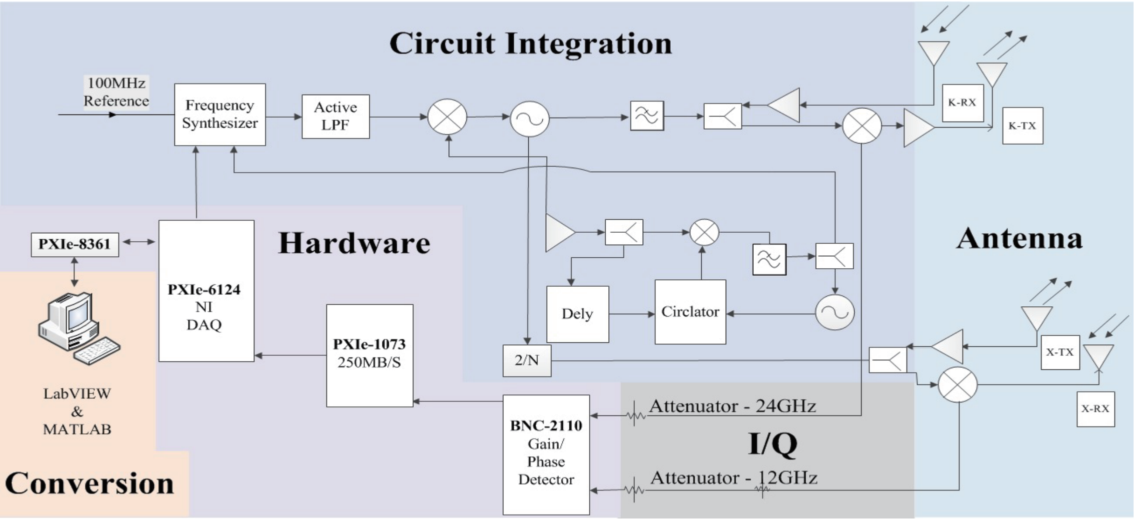

Fig. 2. (Color online) System block diagram of contactless Doppler radar.

based on a PXI Express architecture, integrating the PXIe-1073 chassis and control system with the PXIe-6124 DAQ card, PXIe-8361 interface module, and BNC-2110 sampling module. The resulting I/Q analog signals are routed to the DAQ device for synchronized sampling and time-series recording.

Circuit integration is a core functionality of the proposed system and primarily relies on an integrated frequency synthesizer, which consists of a digital phase-locked loop (DPLL) comprising a phase–frequency detector, an active loop filter, and a VCO. Within the DPLL, the design of the active loop filter directly determines several key characteristics of the phase-locked loop (PLL).(9) This loop filter, which is implemented as an LPF, serves two primary functions. First, it removes high-frequency components from the error signal generated by the phase–frequency detector, which represents the difference between the reference and feedback frequencies, allowing only the DC component to pass through. This DC signal regulates the VCO frequency. Second, the filter prevents AC components from modulating the VCO, thereby reducing sideband frequencies around the carrier and suppressing noise interference. The loop filter also defines the overall loop bandwidth and the PLL's lock acquisition time. Two critical parameters, namely, the time constant and damping factor, govern the filter's effect on the loop. During the locking process, the time constant determines the system response, including the potential overshoot or undershoot of the correction signal and the speed of lock acquisition (12 GH/24 GHz). A smaller time constant accelerates lock acquisition but can compromise stability, whereas a larger time constant improves stability and phase error reduction but slows down lock acquisition. However, excessively increasing the time constant may extend the lock time beyond practical limits, preventing the PLL from achieving lock. Therefore, the time constant must be selected such that system specifications are met. To further enhance stability, the PLL architecture incorporates a low-noise reference frequency source, namely, the CCHD-950-50-100M (Crystek) device, which provides a stable reference signal. The active loop filter is implemented using an AD797 LPF, allowing adjustable zero-pole placement, gain, and output swing. This design improves the loop's flexibility and enhances the drive capability of the VCO control voltage.

The PLL is designed in accordance with the overall circuit system architecture. For the active loop filter, the VCO gain (Kvco) was set to 95 MHz/V, the reference frequency was set to 100 MHz, and the loop bandwidth was set to 10 and 100 kHz. This configuration allows the determination of phase margin and closed-loop gain. The measured signals are shown in Fig. 3.

When the main beam of the proposed radar system is directed toward the radial artery near the human wrist, the primary analysis target is the minor motion of the skin surface, which produces time-varying echo phase variations. According to the measurement principle of the proposed system, an echo is generated when electromagnetic waves are transmitted toward a reflective target that is not composed of absorptive material. Distinctive features in this echo signal indicate specific changes in the target. When the target moves at a constant velocity, the carrier frequency of the echo shifts, which is known as the Doppler effect. In near-range conditions, where the target microdisplacement is considerably smaller than the wavelength, the phase change of the echo can be approximated as a linear function of microdisplacement. Consequently, phase demodulation enables the extraction of the periodic signal corresponding to

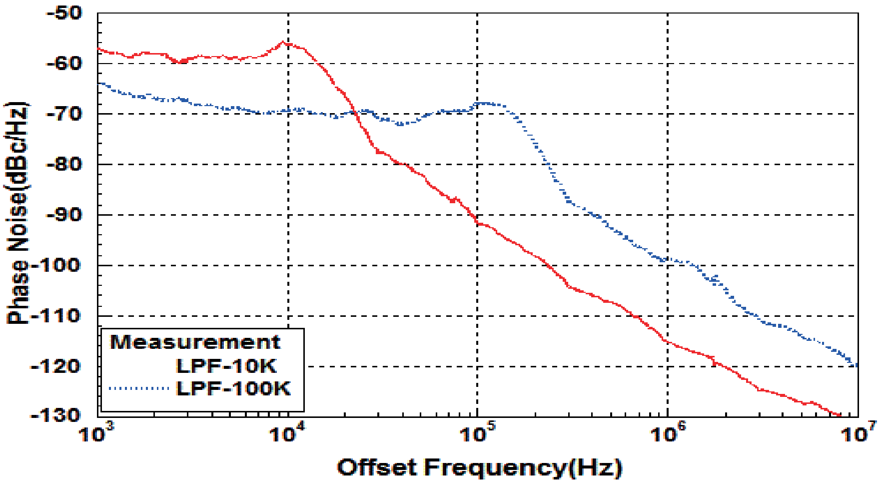

Fig. 3. (Color online) Measured phase noise versus offset frequency for two loop/control LPF corner frequencies: LPF-10K and LPF-100K.

the pulse. The Doppler frequency shift is determined from the relative velocity between the radar and the target and the wavelength of the transmitted electromagnetic wave. The Doppler frequency shift is expressed in Eq. (1), in which V is the target's velocity relative to the radar and λ is the wavelength of the transmitted wave.

$$f_{KX} = 2V / \lambda_{KX} \tag{1}$$

3. I/Q Reception and Data Collection

3.1 I/Q reception

For pulse measurement, the I- and Q-phase signals are simultaneously acquired using an I/Q reception architecture. This approach enables the reconstruction of the complex baseband echo signal from I and Q components, avoiding signal inversion or distortion that may occur when a single path crosses a zero-phase point. Through vector demodulation, the instantaneous phase and amplitude values are extracted to improve the stability of microdisplacement measurements. In Doppler and microdisplacement measurements, I/Q reception effectively reduces directional ambiguity and extends the effective measurement time.

a) I/Q demodulation: Instantaneous phase, phase difference, and amplitude information are derived from I- and Q-phase signals to track microdisplacement.
b) Denoising and motion artifact removal: Low-frequency body motion and environmental drift are low-pass-filtered while preserving the primary pulse frequency and its harmonic structure.
c) Frequency and waveform estimation: The fast Fourier transform (FFT) is used to estimate the primary pulse frequency, whereas the wavelet transform (WT) is employed to enhance nonstationary pulse waveform features and improve the visibility of characteristic points.

d) Output of HR and PR values: PR and HR values are derived from the 24 and 12 GHz measurements, respectively. Dual-band consistency checks, such as frequency agreement and phase or energy credibility thresholds, enhance the reliability of the final output.

In the proposed dual-band measurement setup, both antenna arrays are aligned at a fixed distance from the measurement point. The antenna boresight direction and the angle between the antenna normal and the target surface are mechanically constrained to ensure that echo fluctuations caused by angular deviations remain within a controllable range. The proposed system leverages the Doppler effect to extract physiological signals. The radar transmitter (Tx) emits a CW carrier, which is reflected from the target and received at the radar receiver (Rx). Pulse-induced microdisplacement [$x(t)$] modulates the phase of the reflected signal, which is demodulated with the transmitted signal by using a mixer to recover the pulse frequency. The transmitted signal $T(t)$ is defined in Eq. (2), in which f and $\phi(t)$ denote the oscillation frequency and phase noise, respectively. The total distance of a complete measurement path at time t [$2d(t)$] is defined in Eq. (3), in which the baseline path distance and pulse-induced microdisplacement are represented by $2d_0$ and $2x(t)$, respectively. The received signal $R(t)$ is expressed in Eq. (4).

$$T(t) = \cos(2\pi ft+\phi(t)) \tag{2}$$

$$2d(t)=2d_0 + 2x(t) \tag{3}$$

$$R(t) = \cos\left[2\pi ft - \left(t - \frac{2d\left(t - \frac{d(t)}{c}\right)}{c}\right) + \phi\left(t - \frac{2d\left(t - \frac{d(t)}{c}\right)}{c}\right)\right] \tag{4}$$

The I- and Q-phase signal components are recombined to reconstruct the signal phase. To prevent the distortion of physiological signals during measurement, an I/Q receiver is employed to reduce the occurrence of invalid detection points. The local oscillator input is split into signals P_I and P_Q, which have the same amplitude but a phase difference of 90°. Each of these signals is mixed with the received signal $R(t)$ to generate baseband outputs as follows.

$$P_I(t) = \cos\left[\theta + \frac{4\pi x(t)}{\lambda} + \frac{4\pi y(t)}{\lambda} + \Delta\phi(t)\right] \tag{5}$$

$$P_Q(t) = \sin\left[\theta + \frac{4\pi x(t)}{\lambda} + \frac{4\pi y(t)}{\lambda} + \Delta\phi(t)\right] \tag{6}$$

Because I/Q signals are orthogonal, when the I-channel output corresponds to an invalid detection point, the Q-channel provides the optimal measurement. Similarly, when the Q-channel output is invalid, the I-channel provides the valid measurement. This design is intended to prevent signal distortion caused by invalid detection points in the output. To enhance

Table 1
Primary functions of different system components by category.

Region (Fig. 1)	Components or tools	Primary function	Output or result
RADAR	24 GHz: SAM-2432432212-KF-L1 (phased Tx and Rx antennas) 12 GHz: SWC-90SF-R5 (conical Tx and Rx antennas)	Noncontact echo transmission and reception as well as microdisplacement or Doppler measurement	I/Q baseband echoes (I- and Q-phases)
Hardware	System Control Unit	Measurement workflow control, parameter configuration, and data management	Control commands and measurement records
Circuit integration	DAQ: PXIe-1073, PXIe-6124, PXIe-8361, BNC-2110	Synchronized acquisition and transfer of I/Q signals	Raw I/Q data files
	Local oscillator distribution, mixing and demodulation, isolation and filtering, and calibration	Dual-frequency link integration, reduced coupling, and I/Q usability assurance	Stable I/Q output with reduced distortion
Software	LabVIEW	Real-time signal acquisition, signal monitoring, and data logging	Traceable I/Q database
	MATLAB	I/Q demodulation → denoising and motion artifact removal → FFT and WT→ HR and PR estimation	HR and PR values, spectra and 12 and 24 GHz time-domain waveforms, and confidence metrics

robustness under body motion and environmental noise, the FFT is used for primary-frequency estimation, whereas the WT is employed for time–frequency analysis and feature extraction. This dual approach enables the system to preserve both frequency accuracy and waveform morphology, facilitating the subsequent analysis of pulse waveform features (e.g., the rising edge, reflection waves, and notches) and the advanced estimation of circulatory indices. Table 1 shows the primary functions, outputs, and results of different system components.

3.2 I/Q baseband reconstruction and phase demodulation

In this section, we describe the integration of the PLL and VCO. An integer-N PLL (PE3336) is employed in combination with the HMC739LP4 to generate the frequency sources and signal paths required for the 24 and 12 GHz antenna arrays. The MC739LP4/739LP4E VCO serves as a high-frequency oscillator, providing an operational range of 24–26 GHz. Its output acts as a coherent source, with isolation and power distribution applied to control frequency. A dual-frequency cross-validation strategy is implemented by the proposed system. If the 24 GHz band is heavily affected by posture changes or reflection interference, the 12 GHz echo is used as a reference to determine whether to de-emphasize or ignore the segment in estimation. Similarly, if the 12 GHz band is affected, the 24 GHz echo serves as the reference. This dual-frequency complementary approach increases the proportion of usable measurement segments. For I/Q demodulation and phase or microdisplacement estimation, both the 24 GHz (SAM-2432432212-KF-L1 phased antenna array) and 12 GHz (SWC-90SF-R5 conical antenna array) systems employ an I/Q reception architecture to simultaneously acquire the I and Q signals (Fig. 4).

Human pulse activity induces microscale fluctuations and microdisplacements of the wrist skin and arterial wall, which cause variations in the echo phase. Accordingly, the received signal is represented as a complex baseband signal. To achieve accurate phase demodulation, an arctangent operation is applied to the I/Q output data. The I- and Q-channel outputs maintain a constant phase relationship and represent the cosine and sine components of the received signal, respectively. The static phase offset reflects the distance between the measurement system and the target, and the time-varying phase shift exhibits a linear relationship with the measured chest microdisplacement. Consequently, accurate phase demodulation can be achieved regardless of the target position. The arctangent-based phase extraction from the I- and Q-channel outputs is expressed in Eq. (7). Several complementary methods are employed for frequency estimation and waveform reconstruction. The FFT is applied to motion-suppressed signals to identify the dominant spectral peak corresponding to the PR (i.e., to estimate the primary frequency). To address the limited frequency resolution of the FFT for short time

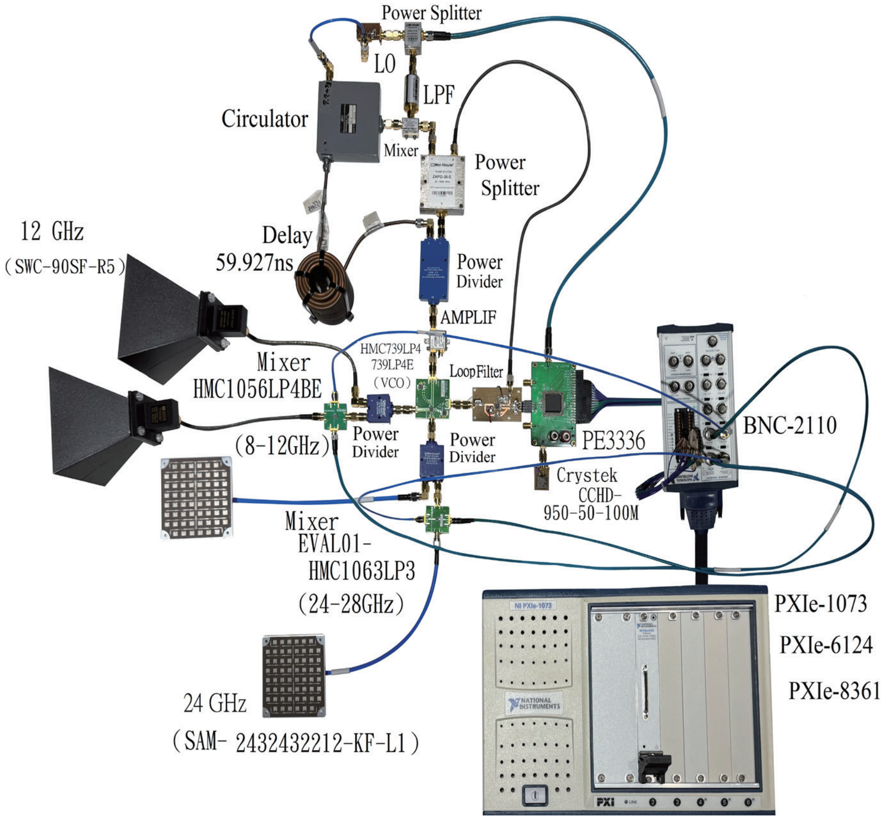

Fig. 4. (Color online) Hardware implementation and measurement platform of the proposed dual-band (12 and 24 GHz) contactless CW Doppler radar system.

windows, autocorrelation and interpeak-interval-based methods are used in the time domain to estimate the pulse period. In addition, wavelet-based time–frequency analysis supports the tracking of short-term PR variations and facilitates discrimination between respiratory and pulse components. During PR estimation, the pulse waveform morphology is preserved to enable subsequent feature-point analysis for factors such as rise time, relative pulse amplitude variation, and waveform symmetry. The superposition of the phase information associated with respiratory or pulse signals [$p(t)$] is expressed in Eq. (8). On the basis of the measured I-channel signal, the circuit architecture divides the VCO output into two paths. A phase difference is introduced by a delay line with a time constant τ, following which the two signals are mixed to extract noise components. Accordingly, the VCO output is modeled as an ideal signal ($w_c t + m(t)$), whereas the delayed signal is represented as $\sin(w_c(t-\tau) + m(t-\tau))$. These two signals, which have a phase difference of 90°, are fed into a mixer and then passed through an LPF to remove high-frequency components, which enables the extraction of noise terms originating from the VCO. Applying product-to-sum operations yields Eq. (9). After low-pass filtering within the circuit, the high-frequency terms in the leading component are attenuated, resulting in the expression presented in Eq. (10). Because the remaining terms are small, this expression can be simplified as Eq. (11), in which the first and second terms represent a constant value and the demodulated VCO phase noise, respectively. The constant term is removed through DC blocking; thus, Eq. (12) is obtained. This equation can be used to determine the VCO phase noise (Figs. 5 and 6).

$$\phi(t) = \arctan\left(\frac{B_Q(t)}{B_I(t)}\right) = \arctan\left(\frac{\sin(\theta + p(t))}{\cos(\theta + p(t))}\right) = \theta + p(t) \tag{7}$$

$$p(t) = \frac{4\pi(x(t) + y(t))}{\lambda} \tag{8}$$

$$V_{out}(t) = \sin(\omega_c(t-\tau) + n(t-\tau)) \cdot \cos(\omega_c t + m(t) \tag{9}$$

$$V_{out}(t) = \frac{1}{2}\sin(2\omega_c t - \omega_c\tau - m(t)\tau + 2m(t)t + s(t)) + \frac{1}{2}\sin(-\omega_c\tau - n\tau - s(t)) \tag{10}$$

$$V_{out}(t) = \frac{1}{2}\sin(-\omega_c\tau - m(t)\tau - s(t)) \tag{11}$$

$$V_{out}(t) \approx \frac{1}{2}\left[-m(t)\tau - s(t)\right] \tag{12}$$

To ensure alignment and consistency across all signal processing stages in this study, the measurement procedure was divided into two steps: distance measurement and localization measurement. Radar echo signals with frequencies of 12 and 24 GHz were first transformed into the range domain to identify the distance intervals in which the dominant reflected energy was concentrated. Dual-frequency measurements were then used to localize differences in echo responses between the two bands (Figs. 5 and 6). The identified distance intervals served as range gates for subsequent pulsation signal acquisition. During pulse measurement with CW and

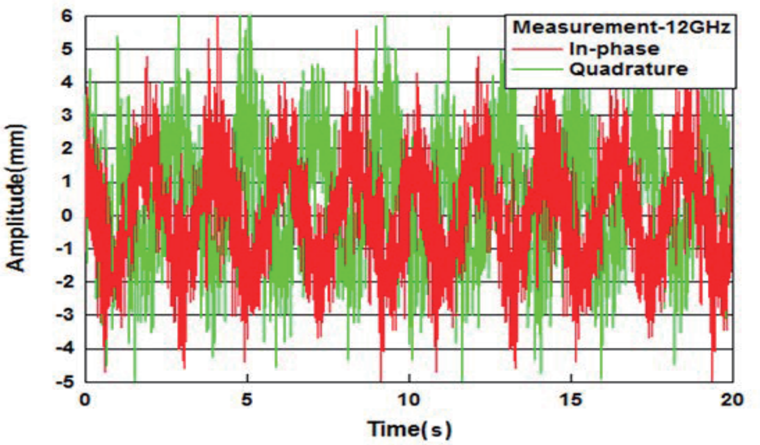

Fig. 5. (Color online) Time-domain in-phase (I) and quadrature (Q) baseband signals measured at 12 GHz. These raw I/Q sequences are used for subsequent complex demodulation and phase-based microdisplacement reconstruction for pulse/respiration extraction.

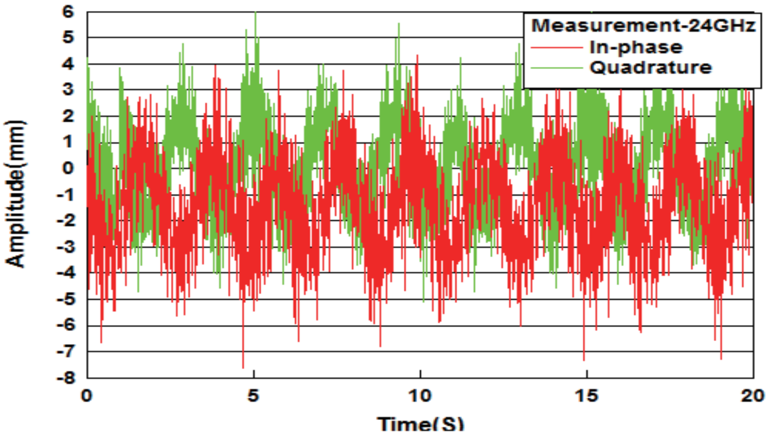

Fig. 6. (Color online) Time-domain in-phase (I) and quadrature (Q) baseband signals measured at 24 GHz. These raw I/Q sequences are used for subsequent complex demodulation and phase-based microdisplacement reconstruction for pulse/respiration extraction.

quasi-CW radar configurations, microscale microdisplacements of the skin surface induced Doppler frequency shifts. The dominant frequency components were extracted through frequency-domain analysis, mapped to the time domain, and then converted into PR estimates. As illustrated in Figs. 7 and 8, under identical measurement conditions, the primary energy peaks of both frequency bands occurred within similar distance ranges, indicating that the two bands captured echoes from the same target region. In addition, differences in peak amplitude and sidelobe noise floors existed between the two bands, reflecting variations in measurement sensitivity attributable to differences in operating frequency, scattering characteristics, and penetration behavior.

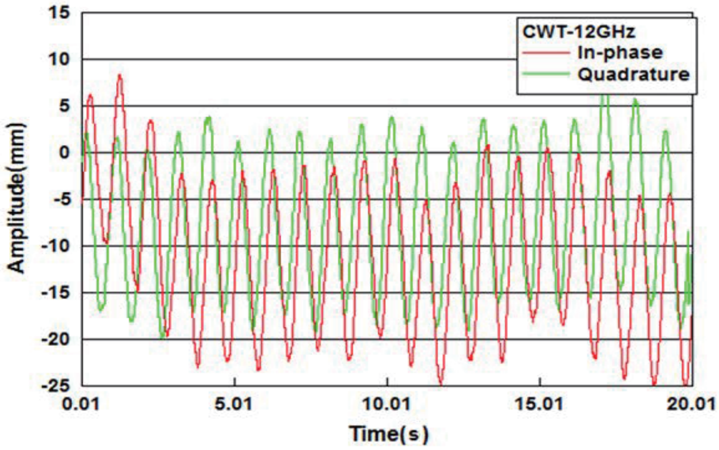

Fig. 7. (Color online) Time-domain in-phase (I) and quadrature (Q) signals at 12 GHz after WT-based denoising/band selection.

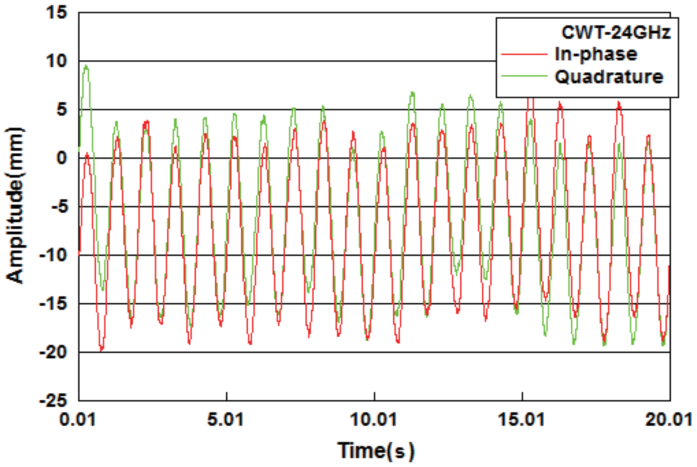

Fig. 8 (Color online) Time-domain in-phase (I) and quadrature (Q) signals at 24 GHz after WT-based denoising/band selection.

3.3 Heartbeat event extraction using FFT and WT in juxtaposition with ECG

After establishing the range gates, we performed time–frequency analysis on the gated echo sequences to extract heartbeat- and pulse-related components. Because cardiac signals are inherently nonstationary—exhibiting cycle-to-cycle variations in amplitude and frequency content—time–frequency representations such as the short-time Fourier transform and WT enhance signal discrimination capability under noise and interference. Related studies have shown that the WT effectively reduces estimation error and improves the extraction of cardiac components in radar-based vital-sign monitoring. Accordingly, in this study, we first identified the dominant frequency band through Fourier-domain analysis and then applied the WT to reinforce transient structures. This process resulted in the conversion of continuous measurement sequences into clearly identifiable heartbeat event sequences, which were analogous to QRS-related features in ECG data.(10) To ensure a valid juxtaposition with the ECG reference signal,(11) the temporal misalignment caused by asynchronous internal clocks across devices must be addressed.(12) Li and Lin reported that when ECG and radar systems rely on different internal clocks, clock drift should be mitigated by first estimating the effective sampling rate through FFT-based analysis and then conducting resampling to a unified temporal resolution.(13) Subsequently, the optimal temporal offset is determined from the peak of the cross-correlation function and compensated within the radar time series to achieve synchronization. As illustrated in Fig. 9, after temporal alignment, the pulsation features extracted from the 12 and 24 GHz radar signals exhibited periodicity and event timing consistent with ECG heartbeat cycles, confirming that the dual-band radar system reliably tracked cardiac periodicity (Fig. 10).

The antenna of the proposed system consists of two components: a K-band (24 GHz) phased antenna array and an X-band (12 GHz) conical antenna array. The 24 GHz phased antenna array acquires and then mixes transmitter (Tx)/receiver (Rx) phase signals. Although the 24 GHz band shows a shallower penetration than the 12 GHz one does, the 24 GHz band is optimized for microdisplacement sensitivity, thus enhancing near-field phase detection. The 12 GHz conical antenna array captures Tx/Rx signals to increase measurement coverage and penetration. Signals from the two bands provide complementary information. The radar circuit system contains a frequency synthesizer with low phase noise. The front end of this synthesizer integrates an integer-N synthesizer with an actively tuned loop filter, allowing precise frequency adjustments and facilitating integration into the proposed dual-frequency physiological Doppler radar system. A high-frequency, microwave VCO paired with the active loop filter delivers a

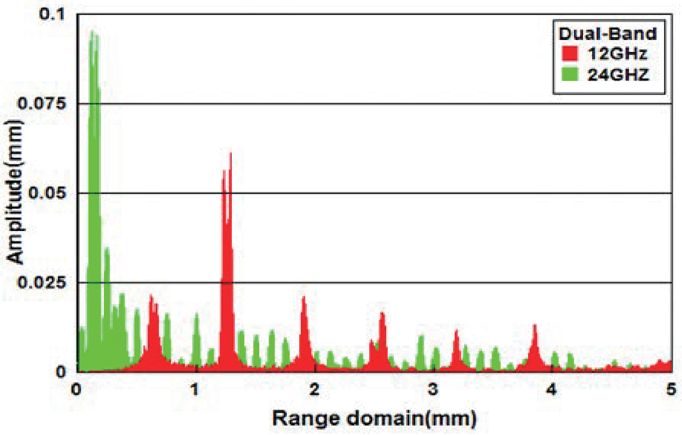

Fig. 9. (Color online) Range-domain magnitude profiles of dual-band radar signals (12 and 24 GHz). The peaks indicate dominant reflection bins, which are used for range-bin selection prior to physiological signal extraction.

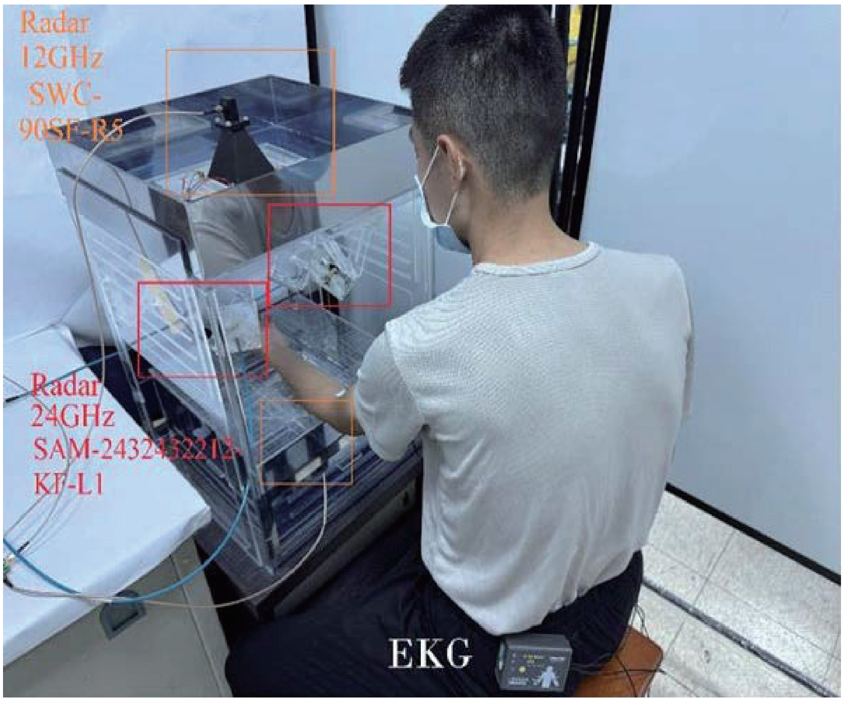

Fig. 10. (Color online) Experimental setup for synchronized dual-band (12/24 GHz) contactless Doppler radar measurement with ECG (EKG) reference.

stable output of 24–26 GHz. The radio frequency/2 path is obtained by frequency division from the VCO output to integrate the 12 GHz antenna, thereby completing the second antenna array. Signal acquisition is performed through a framework that integrates in-phase and quadrature (I/Q) reception. Individually mixed and frequency-divided signals from the 24 and 12 GHz bands are captured using an NI PXIe-1073 chassis with an NI PXIe-6124 data acquisition card, supplemented by NI PXIe-8361 and NI BNC-2110 modules. The I- and Q-phase signals are subjected to I/Q demodulation, followed by noise and interference removal as well as frequency and waveform estimation. Pulse and heart rates are derived from Fourier and wavelet transforms, which enable dual-frequency cross-validation and support physiological parameter comparison through correlation analysis. This dual-frequency approach offers complementary advantages under varying conditions, enhancing signal robustness and interference resilience and demonstrating feasibility for noncontact physiological monitoring and pulse measurement. Experimental results indicated that the 24 GHz antenna array provides high sensitivity to microdisplacement-induced phase variations, whereas the 12 GHz antenna array offers deep penetration through clothing and body tissue. The synchronized dual-frequency measurements of the proposed system provide complementary data, supporting reliable noncontact physiological monitoring and pulse measurement. In this study, the 12 and 24 GHz I/Q signals were not directly summed during signal combination. Instead, a dual-band parallel processing framework was employed, with each frequency band independently subjected to I/Q demodulation, denoising, band-pass filtering, body motion suppression, FFT analysis, and wavelet analysis, and then used for HR or PR estimation. The resulting outputs obtained with both bands were then compared, and similar results were fused to enhance measurement robustness. The aforementioned processes are described as follows (Fig. 11).

a) Dual-band parallel I/Q demodulation: Complex I/Q signals from the 12 and 24 GHz channels are subjected to independent phase and microdisplacement demodulation, which produces two sets of microdisplacement and phase sequences.
b) Denoising, band-pass filtering, and body motion suppression: Each sequence is subjected to denoising, band-pass filtering, and body motion suppression to remove low-frequency drift and nonphysiological interference. These procedures enhance the detectability of the physiological signals.
c) Frequency and waveform estimation: Within a fixed observation window, FFT and wavelet transform are applied to each sequence to estimate the dominant physiological frequency components. This process yields HR or PR signals as well as quantitative indicators such as main-peak energy, signal-to-noise ratio, spectral peak prominence, and peak-amplitude differences.
d) Dual-band cross-validation and data fusion: The consistency between the dual-band estimation results serves as the basis for quality control and fusion. When the HR or PR estimates from the 12 and 24 GHz channels exhibit acceptable differences or when their time-domain waveforms show strong correlation, the corresponding segment is considered reliable, and the fused HR or PR estimate is reported. If only one band satisfies the quality threshold, that band supplies the output. If both bands fail to satisfy the threshold or they exhibit inconsistent results, the segment is labeled unusable to prevent misestimation caused by motion artifacts or noise.
e) Consistency evaluation: Pearson correlation analysis is employed to quantify the consistency between the dual-band waveforms and estimation results, which serves as an objective

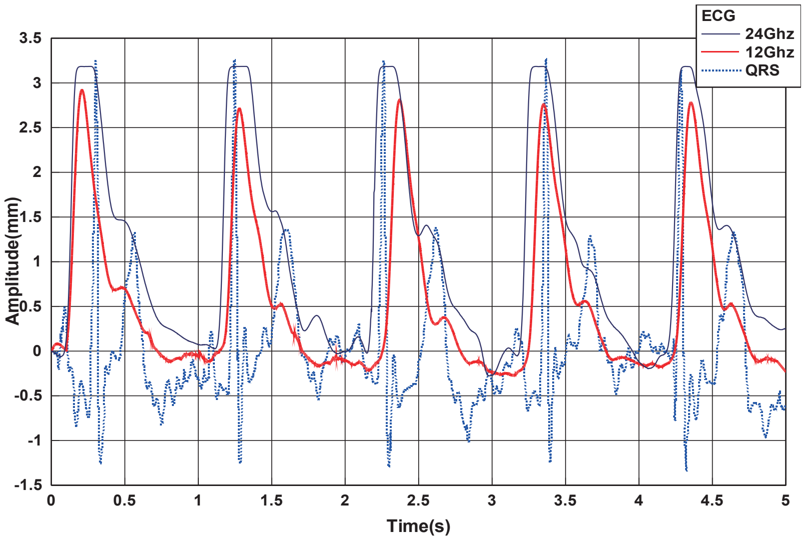

Fig. 11 (Color online) Time-aligned overlap plot of microdisplacement signals.

indicator for cross-validation. In addition, pulse transit time, defined as the time difference between the pulse-wave peak and the ECG peak, is extracted directly from the raw data without the application of a moving average.

After I/Q demodulation, the phase information was transformed into a time series representing microdisplacement or pulsation waveforms. Delay compensation was then applied. This step is critical because the ECG R-peak timing and the radar-derived waveform can exhibit a systematic time offset introduced by the measurement circuitry and acquisition chain. After compensating for this relative delay, the Pearson correlation coefficient r between the ECG-derived reference sequence (R-peak-based) and the radar-derived physiological waveform typically increases substantially. In radar-based measurements, mechanically induced pulsations typically lag behind the R peaks of the ECG signal. Therefore, the optimal time delay was estimated through cross-correlation analysis by using Eq. (13), in which A_x and A_k denote the 24 and 12 GHz signals, respectively. Because radar-derived pulsation signals generally exhibit periodic behavior synchronized with cardiac activity, we conducted band-consistent processing, which involved analyzing the pulsation signal as a time-varying sequence within a predefined frequency band by using Eq. (14). Moreover, pulsation signals from both the X- and K-band radars were processed over the same frequency range [Eq. (15)]. The fundamental HR bands (min–max) of the X- and K-band signals were then used to compute the correlation coefficient γ [Eq. (16)]. Notably, the analysis focused on a pulse-related correlation band rather than being restricted to the fundamental HR frequency $\mathcal{H}$ [Eqs. (17) and (18)] alone. Furthermore, energy envelope analysis, which involved the extraction of root mean square values and the energy envelope, was employed to improve the robustness of estimations against noise. This approach effectively captured amplitude trends and facilitated subsequent cross-band (X/K) correlation analysis based on envelope characteristics, thereby enhancing the reliability of pulse signal comparison. In addition, the estimated PR/HR values derived from the dominant spectral peaks were compared across bands as a secondary consistency check.

$$\tau = \arg\max corr(A_x(t), A_k(A(t+\tau)) \tag{13}$$

$$A_{PW}(t) = BPF_{xmin-kmax}(A(t)) \tag{14}$$

$$\mathcal{Y}_{x-kPW}(t) = BPF_{xmin-kmax}(\mathcal{Y}_{x-k}(t)) \tag{15}$$

$$\gamma_{x-kPW}(t) = corr_{xmin-kmax}(A_{PW}(t)\mathcal{Y}_{x-kPW}) \tag{16}$$

$$\mathcal{Y}_{x-kPW}(t) = BPF_{xmin-kmax}(\mathcal{Y}_{x-kPW}(t)) \tag{17}$$

$$A_{x-kPW}(t) = \mathcal{H}(y_{x-kPW}(t)) \tag{18}$$

3.4 Examination of linear consistency through correlation analysis

After range gate extraction, time–frequency transformation, and temporal alignment were completed, Pearson's correlation coefficient (r) was employed to quantify the linear consistency between the 12 and 24 GHz measurement sequences. To facilitate pulse signal identification and stabilize amplitude features, the Hilbert transform was used to extract the envelope amplitude, which was adopted as a key feature for sequence alignment, and $A_E(t)$ was smoothed using a short moving-average window before alignment. $X(t)$ was obtained from the demodulated phase and converted to microdisplacement, followed by drift removal and band-limited filtering, as expressed in Eq. (19).

$$A_E(t) = \sqrt{X(t)^2 + (\mathcal{H}\{x(t)\})^2} \tag{19}$$

The measurement sequences from both frequency bands exhibited highly synchronized amplitude variations, reflecting strong linear consistency. This high degree of agreement provides a robust basis for dual-frequency cross-validation and signal fusion. Following the synchronized measurement procedure, the estimated temporal offset was applied to the radar sequences to achieve final alignment, ensuring time-domain consistency before segment-wise analysis (Fig. 12). In the time-aligned comparison of dual-band radar and ECG, the upper and middle traces show the normalized pulse-related waveforms extracted from the 24 and 12 GHz radar channels, respectively.

A summary of functional roles, inter-band cross-checking (cross-validation), and fusion strategy for the proposed dual-band (24 and 12 GHz) contactless CW Doppler radar system is shown in Table 2. $A_{24PW}(t)$ and $A_{12PW}(t)$ denote the radar-derived pulse-waveform amplitude sequences from the 24 and 12 GHz channels, respectively. The 24 GHz channel provides higher phase sensitivity and waveform resolution for detailed pulse morphology and microdisplacement-related feature analysis, whereas the 12 GHz channel offers improved stability and robustness under posture variation, occlusion, and reflection changes, serving as a reliable baseline for HR/PR estimation and inter-band consistency checking. The fusion strategy adaptively selects the primary band based on channel quality (e.g., I/Q SNR or waveform-quality metrics): the 24 GHz channel is used as the primary source when its quality is high; otherwise, the 12 GHz channel provides more robust HR/PR estimates, while inter-band consistency metrics are used for cross-checking.

Dual-band radar systems have already been implemented in commercially available products. For example, Ainstein LR-D1 Pro is a commercial dual-band (24/60 GHz) radar altimeter that has been applied in unmanned aerial vehicle measurements.(14) Its primary advantage lies in dual-frequency data fusion, which preserves high measurement accuracy and reliability across diverse environmental and weather conditions. For indoor applications, commercially available millimeter-wave radar systems, such as OGA Smart Care (58–61.5 GHz), generally require specific installation heights and site configurations.(15) In environments characterized by obstructions or multipath propagation, these systems may experience overlapping coverage regions or detection blind spots (Table 3).

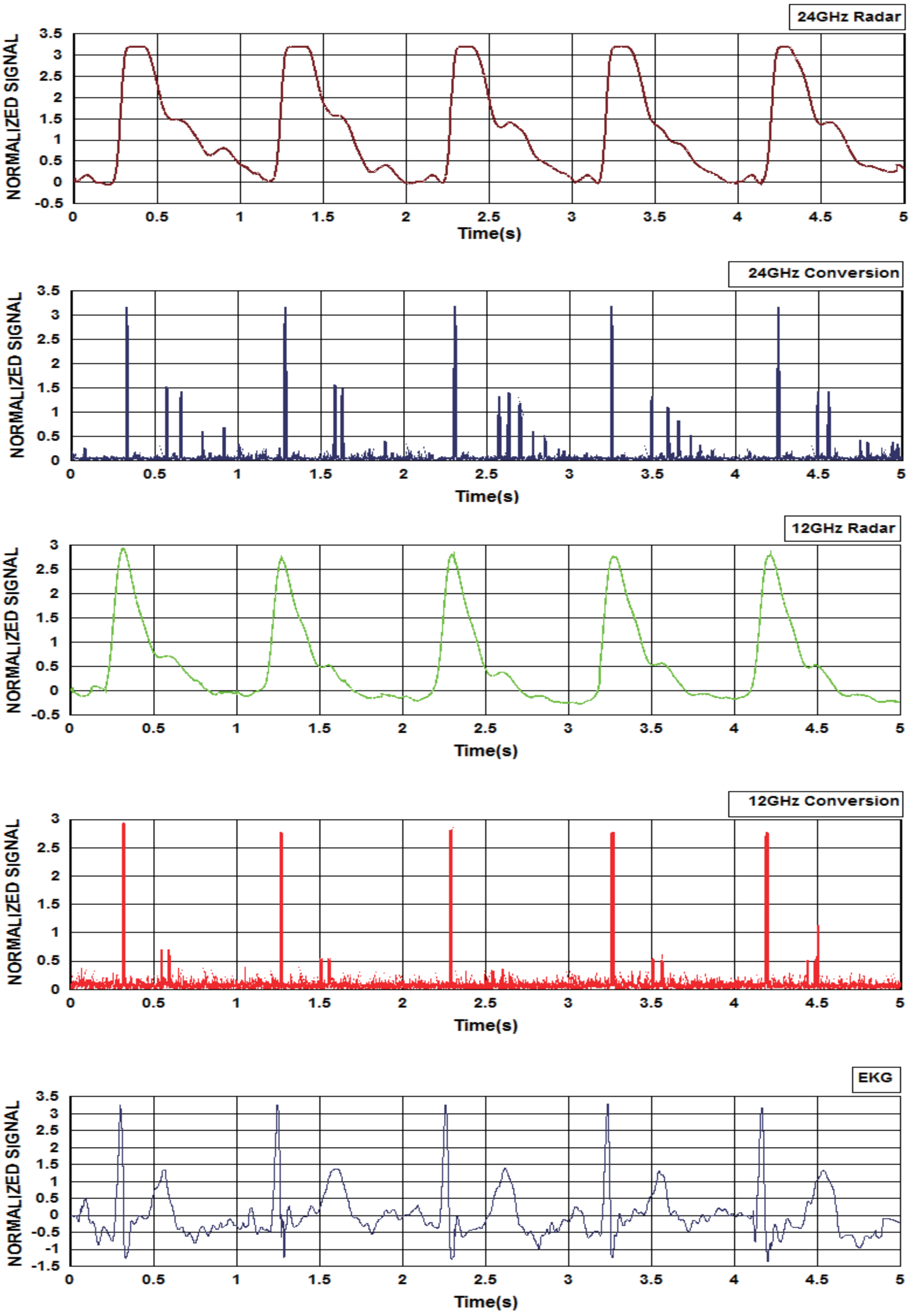

Fig. 12. (Color online) Time-aligned comparison of dual-band radar and ECG. The upper and middle traces show the normalized pulse-related waveforms extracted from the 24 and 12 GHz radar channels, respectively.

Table 2
Summary of functional roles and inter-band cross-checking (cross-validation).

Antenna array	24 GHz RADAR (SAM-2432432212-KF-L1)	12 GHz RADAR (SWC-90SF-R5)
Category	24 GHz amplitude:	12 GHz amplitude:
Primary advantages	High phase sensitivity and pulse waveform resolution	Robust link performance, high directional gain, higher stability under posture variations, and robustness to occlusion and reflection changes
Primary applications	Analysis of pulse waveforms, microdisplacement-induced phase variations, and PR waveform features	Baseline HR or PR estimation as well as cross-validation (12 vs 24 GHz).
Fusion strategy	Estimation of the primary pulse waveform and superficial PR information when the 24 GHz I- and Q-channels are high	Cross-validation and measurement of deeper HR or PR when the 24 GHz I- and Q-channels are low

a) LR-D1 Pro (commercial dual-band radar altimeter): Dual-band radars have been deployed to enhance measurement reliability. For example, Ainstein LR-D1 Pro employs a 24/60 GHz dual-band architecture combined with data fusion to maintain continuous and stable altitude outputs across varying heights and environmental conditions. This device demonstrates that the integration of data fusion into a dual-band architecture can effectively improve system reliability.

b) OGA Smart Care (commercial single-band millimeter-wave physiological sensor): Commercial single-band physiological sensors (e.g., OGA Smart Care; frequency: 58–61.5 GHz) primarily emphasize coverage and event detection. Therefore, these sensors offer a large detection range and angular coverage as well as relevant alert functions (e.g., those related to the detection of human presence, falls, and abnormal inactivity). Although such systems are widely used in various applications, they generally provide system-level outputs rather than research-grade raw I/Q data or waveform-quality metrics, making waveform-level quantitative comparison difficult. Frequency and waveform estimation: The FFT is used to estimate the primary pulse frequency, whereas the WT is employed to enhance nonstationary pulse waveform features and improve the visibility of characteristic points.

c) Proposed 12/24 GHz dual-band system: The proposed dual-band system was developed to achieve the robust measurement of physiological microdisplacement signals. This system processes 12 and 24 GHz signals simultaneously, using cross-frequency consistency as a quality control measure. Segments with consistent results across the two bands are fused to increase confidence. If only one band satisfies the quality threshold, that band supplies the output. Moreover, inconsistent segments are eliminated to prevent misestimation. This strategy improves the reliability of HR or PR estimation and the proportion of usable data segments, particularly under long-term monitoring and noncontact measurement conditions prone to noise and motion artifacts.

Table 3
Architectural features and application characteristics of LR-D1 Pro, the OGA Smart Care device, and the 12/24 GHz dual-band noncontact physiological monitoring system proposed in this study.

Product	LR-D1 Pro	OGA Smart Care	Proposed physiological measurement system
Applications	Aircraft altitude and velocity measurements for vertical take-off and landing, takeoff/landing, and high-altitude maneuvering operations	Smart Care monitoring applications, including presence detection, fall detection, abnormal inactivity detection, alert notifications, and respiration and HR variation monitoring	Research-oriented noncontact physiological sensing platform for detecting pulse- and heartbeat-related body surface microdisplacements, performing I/Q demodulation, and analyzing cross-frequency consistency
Frequency bands	Dual-band: 24 and 60 GHz	Single-band: 58 or 61.5 GHz	Dual-band: 12 and 24 GHz
Engineering rationale for the frequency design	The 60 GHz band provides high precision at low altitudes, whereas the 24 GHz band supports longer-range measurements at higher altitudes; dual-frequency data fusion produces continuous and reliable altitude estimates.	The single-band architecture primarily supports indoor monitoring and alert functions with wide coverage angles and sensing areas.	The 24 GHz band offers high phase sensitivity to microdisplacements, whereas the 12 GHz band offers improved signal stability; cross-frequency consistency enables data validation and fusion, thereby enhancing robustness.
Operational and performance indicators	Altitude range: 0.3–500 m; update rate: 40 Hz; segmentation accuracy: 5 m (field of view optimized for aircraft vertical altimetry)	(1) Installation height: 2.2–2.9 m; detection diameter: 5 m; detection angle: 100°; transmit power: 6 dBm; supply voltage/current: 5 V/50 mA; operating temperature: –20 to 60 °C. (2) Coverage characteristics: detection angle: 100°; sensing range (including the detection radius diameter): 200 cm; stationary monitoring radius: 150 cm; fall detection radius: 70 cm	(1) 24 GHz: sensing diameter: up to 100 m (indoors); 3-dB beamwidth: 12° × 12° (E-plane × H-plane); return loss: 6–8 dB; supply voltage/current: 5 V/50 mA; operating temperature: –40 to 85 °C. The quantitative evaluation indicators are HR or PR errors (0.25-s window), cross-frequency Pearson correlation, and usable segment ratio. (2) 12 GHz: detection diameter: 3–10 m; respiration detection range: 1–5 m; detection range for heartbeat- or pulse-related body microdisplacements: 0.3–2 m.
Output type	Altitude measurements on flight-control interfaces (e.g., CAN and RS-232, RS-422)	System alerts and status outputs	Research-oriented: Baseband I/Q signals (or equivalent phase or microdisplacement sequences), which are then subjected to processing and statistical analysis

4. Implications, Limitations, and Potential Improvements of the System Design

The proposed dual-radar system leverages the complementary characteristics of 12 and 24 GHz measurements to achieve comprehensive signal acquisition for vital-sign monitoring.

Statistical analysis indicated a strong correlation between these measurements, with Pearson's r being 0.82096, the 95% confidence interval being 0.80756–0.83351 (estimated using Fisher's z-transform), and the two-tailed p-value being considerably lower than 0.001. The 24 GHz radar offers high phase sensitivity and waveform resolution, whereas the 12 GHz radar provides a robust measurement link and enables cross-validation. The proposed system, which exhibits low phase noise and incorporates a complete I/Q demodulation workflow, balances resolution and measurement stability, thus enabling subsequent vital-sign measurements, other applications, respiration–heartbeat separation, pulse waveform morphology analysis, and ECG-synchronized timing feature extraction and parameter optimization. Although the 24 GHz radar is highly sensitive to microdisplacement, suboptimal PLL loop design during experiments can propagate phase noise into the demodulated signal, producing distorted waveforms despite high antenna gain. The use of the PE3336 (hardware module/frequency synthesizer) and HMC739LP4 devices (hardware module/frequency synthesizer/pSemi Corporation, San Diego, CA, USA) with an AD797 active loop filter enables adjustable loop parameters, ensuring both low phase noise and rapid lock acquisition. Tx/Rx-separated antenna configurations substantially reduce coupling errors, particularly in the X-band (24 GHz), where coupling-induced DC offsets and saturation can distort I/Q signals and produce spurious phase drifts. To address these problems, the SAM-2432432212-KF-L1 phased antenna array with Tx/Rx separation is employed in the proposed system, thereby enhancing the reliability of downstream demodulation. In the proposed dual-band approach, the 12 GHz (K-band) measurements do not replace the 24 GHz ones; instead, the 12 GHz measurements are used to capture the optimal signal, assess pulse depth, and validate stability. Although 12 GHz signals are less sensitive to phase microdisplacement and offer a lower waveform resolution than do the 24 GHz ones, the deeper penetration of 12 GHz signals ensures a higher usable signal-to-noise ratio under posture variations and multipath effects, supporting cross-validation. Dual-band fusion improves PR tracking continuity and robustness against body motion. I/Q calibration is a standard requirement for long-term coherent I/Q measurements to maintain stable gain/phase balance under temperature drift, particularly to compensate for gain and phase mismatches caused by temperature drift. Therefore, future studies should incorporate routine or automated calibration procedures into the proposed approach. Dual-band fusion also requires precise time synchronization and data alignment to avoid misinterpretation of apparent discrepancies caused by temporal offsets. Overall, under a fixed measurement distance and alignment, 24 and 12 GHz I/Q signals are processed simultaneously in the proposed method through a consistent workflow involving the following steps in sequence: I/Q demodulation, denoising or motion artifact removal, FFT- or WT-based estimation (and RR when applicable), and HR or PR output generation. This workflow enables reliable noncontact pulse measurement. The proposed approach supports the systematic evaluation of local oscillator parameters, improves the reliability and applicability of radar-based vital-sign monitoring, and provides a foundation for the development of clinical systems for the long-term, noncontact monitoring of additional physiological parameters.

Constellation plots were not generated in this study because of the hardware constraints of the proposed system. The passive mixer introduces relatively high insertion loss and therefore requires a high-power LO signal for appropriate operation. To compensate for the link loss beyond the quadrature power divider, an amplifier was inserted downstream to achieve gain compensation. However, when the amplified signal passes through the balun, the resulting baseband I/Q signal amplitudes remain relatively weak because of limitations related to the device's power, bandwidth, and linearity. In addition, the relatively high measurement noise prior to demodulation limits the reliability of constellation plot interpretation. Future developments will focus on the design of filtering and link calibration mechanisms comprising two main components: (1) a baseband filter for constraining the bandwidth of digital signal transmission and performing pulse shaping and (2) a low-pass filter designed to match the low-pass quantization error response after the raw signal is processed through a PLL. Through accurate matching, the quantization noise arising from quantization errors can be effectively suppressed outside the loop bandwidth, thereby improving overall demodulation performance. These limitations will be a key focus of future system improvements. The improved system will then be used to measure multiple physiological parameters, including HR-induced microdisplacement, respiration-induced chest wall microdisplacement, pulse-induced microdisplacement, and thoracic-expansion-induced microdisplacement. These investigations will support the development of a more comprehensive framework for I/Q constellation analysis and quantitative performance evaluation.

Acknowledgments

I sincerely thank Chao Yuan Kuo (Zhende Acupuncture Clinic, Pingtung) for his assistance with pulse-signal measurements and for providing valuable clinical insights into pulse beat characteristics, which greatly supported the data acquisition and interpretation in this study.
The study protocol was reviewed and approved by the National Cheng Kung University Governance Framework for Human Research Ethics (Approval No. 115-0124).

References

1. K. C. Peng, W. L. Wu, and C. H. Huang: IEEE Sens. J. **22** (2022) 12852. https://doi.org/10.1109/JSEN.2022.3179707
2. W. L. Wu, F. L. Huang, C. Y. Guo, and C. Y. Kuo: Proc. 2025 IEEE 14th Global Conf. Consumer Electronics (GCCE) (IEEE, 2025). https://doi.org/10.1109/GCCE65946.2025.11275281
3. Y. Osawa, S. Hata, M. Hori, and T. Dohi : Sens. Mater. **33** (2021)1063. https://doi.org/10.18494/SAM.2021.3142
4. J. Tu, T. Hwang, and J. Lin: IEEE Trans. Microw. Theory Tech. **64** (2016), 1937 https://doi.org/10.1109/TMTT.2016.2560159
5. F. K. Wang, J. X. Zhong, and J. Y. Shih: IEEE J. Electromagn. RF Microw. Med. Biol. **6** (2022) 449. https://doi.org/10.1109/JERM.2022.3214753
6. Espinoso, M. Alfaras, D. Romero, Y. Castillo-Escario, R. Jané, and Z. Haddi: Proc. 47th Annu. Int. Conf. IEEE Engineering in Medicine and Biology Society (EMBC) (IEEE, 2025). https://doi.org/10.1109/EMBC58623.2025.11251791
7. K. M. Chen, D. Misra, H. Wang, H. R. Chuang, and E. Postow: IEEE Trans. Biomed. Eng. **54** (2007) 697. https://doi.org/10.1109/TBME.1986.325760
8. O. Boric-Lubecke, V. M. Lubecke, A. D. Droitcour, B. K. Park, and A. Singh: Doppler Radar Physiological Sensing (John Wiley & Sons, 2015) pp. 69–94 Chap. 4.

9. S. R. Al-Araji, Z. M. Hussain, and M. A. Al-Qutayri: Digital Phase Lock Loops: Architectures and Applications (Springer, 2006).
10. Y. M. Mao and T. C. Chang: Sens. Mater. **32** (2020) 2641. https://doi.org/10.18494/SAM.2020.2804
11. T. S. Heo, C. Kim, J. D. Kim, C. Y. Park, and Y. S. Kim: Sens. Mater. **33** (2020) 2641. https://doi.org/10.18494/SAM.2020.2804
12. W. Pan, J. Wang, J. Huangfu, C. Li, and L. Singh: Electronics Lett. **47** (2011). https://doi.org/10.1049/el.2011.2419
13. M. Li and J. Lin: IEEE Trans. Microw. Theory Tech. **66** (2018) 568. https://doi.org/10.1109/TMTT.2017.2730182
14. Ainstein: https://www.sundance.com/lr-d1-pro/?utm_source=chatgpt.com (accessed March 2026).
15. Ideas-Hatch: https://www.ideas-hatch.com/hatch_smartcare_detail.jsp?id=137 (accessed March 2026).

About the Authors

Wei-Lung Wu received his B.S. degree from Air Force Institute of Technology, R.O.C., in 2007, and his M.S. and Ph.D. degrees from National Kaohsiung University of Science and Technology, Kaohsiung, in 2015 and 2021, respectively. Since 2014, he has been an assistant professor at Air Force Institute of Technology, R.O.C., Kaohsiung. His current research interests include vital-sign sensing techniques and frequency synthesizers.